

arXiv:2505.07622v1 [cs.CV] 12 May 2025

arXiv:2505.07622v1 [cs.CV] 12 May 2025

arXiv:2505.07622v1 [cs.CV] 12 May 2025

arXiv:2505.07622v1 [cs.CV] 12 May 2025

arXiv:2505.07622v1 [cs.CV] 12 May 2025

arXiv:2505.07622v1 [cs.CV] 12 May 2025

arXiv:2505.07622v1 [cs.CV] 12 May 2025

arXiv:2505.07622v1 [cs.CV] 12 May 2025

arXiv:2505.07622v1 [cs.CV] 12 May 2025

arXiv:2505.07622v1 [cs.CV] 12 May 2025



arXiv:2505.07622v1 [cs.CV] 12 May 2025

arXiv:2505.07622v1 [cs.CV] 12 May 2025

arXiv:2505.07622v1 [cs.CV] 12 May 2025

a uniform network for joint task training, the coordination mechanisms of these two tasks still remain under-explored. Specifically, the retrieval and metric localization tasks have different requirements for feature representation granularity, while existing methods [23], [27] attempt to train a single representation that simultaneously satisfies both requirements, leading to conflicts in feature learning and reduced positioning performance.

In this paper, we propose UnifyGeo, a novel unified framework that integrates both retrieval and metric localization techniques to perform LF-CVGL. Unlike previous methods [23], [27] that rely solely on global descriptors, UnifyGeo incorporates both global descriptors and detailed features for enhanced performance. Specifically, we design a unified learning strategy composed of a shared feature encoder and a multi-task loss function. The shared encoder extracts uniform features for both retrieval and metric localization, effectively constructing task associations. On that basis, the multi-task loss function optimizes the shared encoder by simultaneously supervising global and detailed feature representations, ensuring complementary learning effects. The resulting latent features are fed into task-specific heads, enabling both tasks to mutually benefit from the enriched representations. Furthermore, we also propose a re-ranking mechanism guided by a dedicated loss function to refine the selection of aerial images from retrieval candidates. This ensures reliable reference data for metric localization, and further bridges the gap between retrieval and metric localization tasks. The complete hierarchical geo-localization pipeline is illustrated in Fig. 1. Overall, our contributions are as follows:

- We propose UnifyGeo, a novel hierarchical framework that integrates retrieval and metric localization into a unified network for LF-CVGL, operating in a coarse-to-fine manner.
- We propose a unified learning strategy that integrates multi-granularity representations to support our geo-localization pipeline, and foster mutual enhancement between retrieval and metric localization tasks.
- We introduce a re-ranking strategy guided by a dedicated loss function to refine image retrieval results and provide better references for metric localization, further enhancing the positioning accuracy.
- Extensive experiments demonstrate that UnifyGeo significantly outperforms existing methods on LF-CVGL, and our retrieval and metric localization units within UnifyGeo achieve comparable or better performance than state-of-the-art individual techniques.

II. RELATED WORK

A. Cross-view Image Retrieval

Lin et al. [28] and Workman et al. [29] introduce the first approaches that use image embeddings to address cross-view geo-localization task as a retrieval problem. Compared to earlier approaches using handcrafted features [30], [31], they demonstrate the superiority and great potential of deep learning in this domain. Both approaches employ standard fully connected layers to aggregate local CNN features for

retrieval tasks. To improve aggregation strategies, Hu et al. [16] introduce learnable NetVLAD layers [32] to map CNN features to global descriptors. However, direct aggregation of CNN features fail to reduce the visual differences between cross-view images. To address this, Shi et al. [1] apply a polar coordinate transformation to convert aerial images into a format visually similar to ground views, enabling the network to learn more consistent descriptors. Lin et al. [33] propose learning view-invariant keypoints to eliminate the domain gap at the feature level. Although these transformations improve retrieval performance by narrowing the domain gap, their effectiveness is primarily limited to one-to-one, center-aligned cross-view image matching.

To evaluate cross-view geo-localization in a more realistic setting, Zhu et al. [23] introduce the concept of semi-positive aerial images, which cover the same ground scene from different, non-central viewpoints. In response to these challenges, some approaches have shifted away from coordinate transformation techniques and leverage novel architectures. Zhu et al. [17] and Yang et al. [34] are among the first to utilize the global information modeling capabilities of transformers to learn discriminative representations. Furthermore, Zhang et al. [35] propose a novel approach that decouples content features from spatial layouts, using transformer layers to focus on spatial relationships. Additionally, Zhu et al. [36] introduce a new architecture based on Multi-Head Attention (MA), specifically designed for geo-localization tasks. Deuser et al. [18] simplify the dual-branch architecture into a siamese feature encoder, enhancing the representation power of the global descriptor with a ConvNeXt-base model and global hard sample mining strategies, achieving state-of-the-art retrieval performance. More recently, Shugaev et al. [37] focus on optimizing for limited Field of View (FoV) cases. Li et al. [38] explore unsupervised frameworks for real-world scenarios, although their retrieval performance lags behind that of supervised methods.

B. Cross-view Metric Localization

Given a ground-level query image and an aerial image covering its surrounding environment, the goal of metric localization is to determine the precise position, and when the orientation is also estimated, this task is commonly referred to as pose estimation. In [23], Zhu et al. introduce the first dataset to evaluate this task and propose to regress query position by reusing global descriptors. Subsequently, Xia et al. [24] formulate the task as a multi-class classification problem and further improve the localization performance using a hierarchical matching approach [39]. Chen et al. [40] also utilize matching-based techniques, generating location heatmaps for precise localization in lunar exploration. Instead of letting the network automatically learn matching patterns, Lentsch et al. [26] pre-generate multiple hypothesized pose templates and create a set of map representations for the aerial images based on these templates. The final ground pose is determined by matching features from the query image to those from the map representation set. Shi et al. [25] propose an iterative framework for pose estimation, which projects

aerial image features into the ground-view perspective via homography and refines the query pose using the Levenberg-Marquardt algorithm. More recently, researchers have utilized Bird's Eye View (BEV) transformations, achieved through Vision Transformers [41] or spherical transforms [42], to close the domain gap between ground and aerial views. The mapped BEV feature maps are then densely compared to aerial feature maps for pose estimation. In contrast to existing metric localization methods, which are limited to localizing queries within a local area, our hierarchical geo-localization framework enables accurate geo-localization over large-scale scenarios.

C. Large-scale Fine-grained Cross-view Geo-localization

To achieve LF-CVGL, Zhu et al. [23] propose a model that generates global descriptors for cross-view pairs, using them for both image retrieval and location regression. However, these global descriptors lack fine-grained scene information, limiting localization accuracy [24]. In response, Li et al. [27] introduce local and multi-scale knowledge through an auxiliary image-to-patch retrieval task to enhance cross-view feature representation, and perform localization with location regression similar to [23]. In contrast, our unified learning strategy enables the feature encoder to learn multi-granularity features for geo-localization tasks, and our re-ranking refines image retrieval results to inform metric localization, ultimately achieving robust and accurate hierarchical cross-view geo-localization over large-scale scenarios.

III. METHODOLOGY

In this section, we first explain the task of LF-CVGL (Section III.A) and our hierarchical geo-localization pipeline (Section III.B). We then introduce the key components of our proposed framework UnifyGeo (Section III.C) and the re-ranking mechanism (Section III.D). Finally, we describe the training process of UnifyGeo in detail (Section III.E).

A. Problem Formulation

Considering an aerial database $\mathcal{A} = \{I_a^1, \dots, I_a^N\}$ of N aerial/satellite images, each covering a square region associated with a different geo-location. The N square regions form a complete map representation that covers all possible query locations. With database \mathcal{A} as reference, given a ground-level query image I_g , we aim to estimate the geographic location, $\mathbf{P} = (\hat{x}, \hat{y})$, of camera that took I_g . Here, (\hat{x}, \hat{y}) is the image coordinate in a geo-tagged aerial image of known spatial resolution that covers the query image's camera location.

B. Proposed Hierarchical Pipeline for LF-CVGL

To achieve accurate geo-localization in large-scale scenarios, we employ a hierarchical framework that performs the geo-localization process in a coarse-to-fine manner. As illustrated in Fig. 2, our pipeline can be summarized as follows.

Prior Retrieval. To quickly narrow the geo-localization scope, image retrieval is performed by matching the global descriptors between the query image and the aerial database.

Formally, given global descriptors v_g and v_a^i of I_g and $I_a^i \in \mathcal{A}$, the retrieval task can be formulated as:

$$\begin{aligned} C_k &= \{I_a^{i_1}, \dots, I_a^{i_k}\} \\ &= \arg \min_{I_a^{i_1}, \dots, I_a^{i_k} \in \mathcal{A}} \{d(v_g, v_a^{i_1}), \dots, d(v_g, v_a^{i_k})\}, \end{aligned} \quad (1)$$

where $d(\cdot, \cdot)$ denotes the L_2 distance. This process can be efficiently solved using the k -nearest neighbors (NN) search. The output is a set of k aerial image candidates, denoted as C_k , which are the most likely to cover the query location.

Re-ranking and Location Estimation. To accurately predict the location of the query image, we need to identify the geographically matched candidate image from C_k that truly covers the query location. To achieve this, we predict a discrete probability distribution of the query location over $L \times L$ aerial image pixels for each candidate image. Finally, we re-rank all candidates by combining the initial matching scores of the detailed features associated with the Maximum A-Posteriori (MAP) pixels in each distribution with their retrieval scores. The candidate image with the highest overall score is regarded as the true geographic match for the query image, while the corresponding pixel position with the highest probability is considered as the final predicted query location $\hat{\mathbf{P}}$.

C. UnifyGeo Architecture

UnifyGeo consists of three primary components: the multi-granularity feature encoder, the feature aggregator, and the localization decoder, as illustrated in Fig. 2. The multi-granularity feature encoder extracts two distinct feature maps, each being tailored to address specific tasks. The feature aggregator processes one feature map to generate a global descriptor for image retrieval, while the other feature map is used to extract detailed features for both re-ranking¹ and metric localization.

Multi-granularity Feature Encoder. Due to the natural differences in image characteristics across views, our feature encoder is a pseudo-Siamese network with two branches for ground and aerial views. Within each branch, we introduce two distinct processing pathways that share a single encoder for uniform feature computation.

Formally, given a ground query image I_g and an aerial image $I_a \in \mathcal{A}$ with sizes $H \times W \times 3$ and $L \times L \times 3$, the shared encoders of the two branches first map them into feature maps $\{F_g^i\}$ and $\{F_a^i\}$, where $i \in \{n, \dots, 1\}$ and n corresponds to the number of encoder stages. Then, for the aerial view branch, the multi-granularity feature extractor heads act on top of the last stage's outputs F_a^1 . Specifically, the fine-grained extractor head (denoted as F-head in Fig. 2) further enriches the image representation and produces a detailed feature map F_a^0 with dimension $L' \times L' \times C$. The semantic extractor head (denoted as S-head in Fig. 2) also takes F_a^1 as its input to extract semantic-level latent features G_a , which are then processed by our feature aggregator to generate a global descriptor v_a for the aerial image. Similarly, the ground image branch obtains

¹For a clearer exposition of the detailed feature matching process, we will describe the metric localization process in the localization decoder prior to re-ranking, given that both steps rely on the same initial matching results.

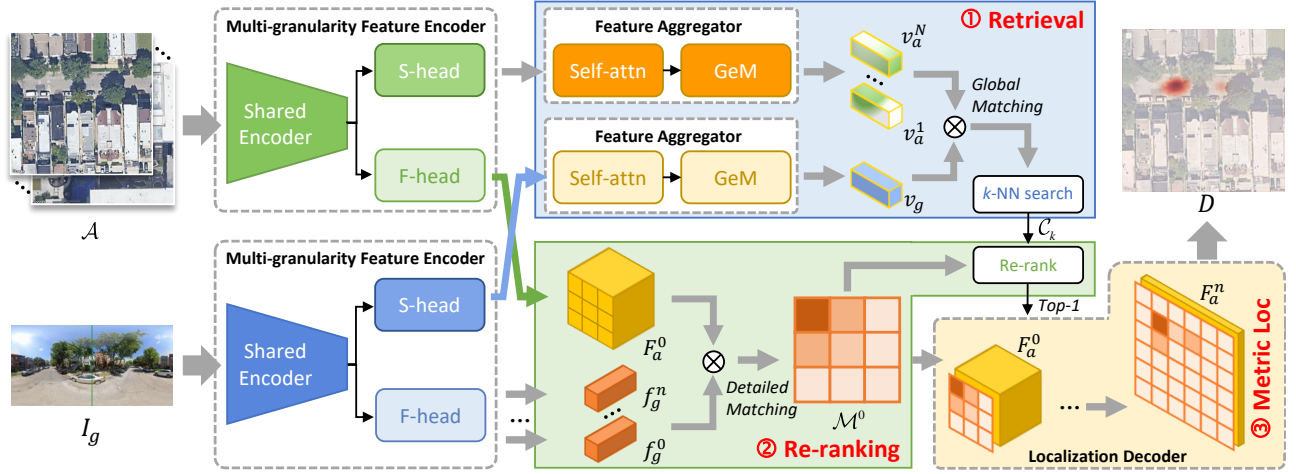


Fig. 2. Overview of our proposed UnifyGeo framework. It consists of separate multi-granularity feature encoders and feature aggregators for the ground and aerial branches, as well as a localization decoder. Given a ground-level query image I_g and an aerial database \mathcal{A} , we first perform cross-view image retrieval (Retrieval) to obtain C_k , a set of k aerial image candidates. These candidates are then re-ranked to select the top-1 matched aerial reference. Finally, cross-view metric localization (Metric Loc) is performed to produce a discrete probability distribution D , which is overlaid on the aerial reference to indicate the likely location of I_g , with deeper red denoting higher probability.

a detailed feature map F_g^0 of size $H' \times W' \times C$ and a global descriptor v_g in the same way. Finally, the global descriptors v_g, v_a are used for retrieval, while the multi-scale feature maps $\{F_a^i \mid i \in \{n, \dots, 0\}\}$ and F_g^0 are used as input for both re-ranking and metric localization.

Feature Aggregator. In UnifyGeo, we design a feature aggregator to extract global descriptors while addressing the potential multi-task conflict in the aerial branch. This conflict arises from the divergent learning objectives of retrieval and metric localization tasks, both of which operate on the same feature maps produced by the shared encoder. Specifically, metric localization requires aligning local regions in the feature map with detailed ground-view descriptors, whereas retrieval demands abstracting the entire feature map into a vector similar to the ground-view global descriptor. To resolve this conflict, we introduce a self-attention mechanism into the aggregator. This mechanism dynamically assigns weights to different features based on their correlation, selectively highlighting the most critical patterns for retrieval while avoiding ineffective aggregation from conflicting features. We further aggregate these critical patterns using generalized mean (GeM) pooling [43], [44], which adjusts the pooling process with learnable parameters to preserve discriminative information in the feature map. Moreover, as not all information in ground images is present in the aerial images (e.g., sky) [26], we also employ the feature aggregator in the ground branch to facilitate the collection of critical representations that can enable contrastive learning with aerial global descriptors.

Concretely, given the features \mathbf{G} produced by the semantic extractor head, \mathbf{G} can either be $G_a \in \mathbb{R}^{L' \times L' \times C}$ or $G_g \in \mathbb{R}^{H' \times W' \times C}$. Each vector $G_{i,j}$ with dimension C located at (i, j) in the spatial direction can be considered as a region descriptor corresponding to a local area of the source image. To capture key semantic information from the global context, the self-attention module first maps region descriptors into a

latent space, generating query (**Q**), key (**K**), and value (**V**) vectors. Then, the process can be represented as follows:

$$\begin{aligned} \mathbf{Q} &= \text{LN}(\mathbf{G}) \mathbf{W}^q, \mathbf{K} = \text{LN}(\mathbf{G}) \mathbf{W}^k, \mathbf{V} = \mathbf{G} \mathbf{W}^v, \\ \Phi &= \mathbf{G} + \text{softmax}\left(\frac{\mathbf{Q} \mathbf{K}^T}{\sqrt{\lambda}}\right) \mathbf{V}, \end{aligned} \quad (2)$$

where $\mathbf{W}^q, \mathbf{W}^k, \mathbf{W}^v$ are linear projection matrices, $\text{LN}(\cdot)$ represents LayerNorm, and λ is a scaling factor. Note that we do not employ multi-head attention, this decision allows us to compute attention based on the full semantics of the region descriptors. Furthermore, we omit the feed-forward network (FFN) commonly found in standard transformer blocks, as it offers only marginal performance improvement at a significant parameter cost [36].

Finally, the enhanced feature map Φ is fed into GeM to generate a single global descriptor v .

$$v = \text{GeM}(\Phi, p) = \left(\frac{1}{H_\Phi W_\Phi} \sum_{i,j \in H_\Phi, W_\Phi} \Phi_{i,j}^p \right)^{\frac{1}{p}}, \quad (3)$$

where p is a learnable parameter that represents the generalized mean power, H_Φ and W_Φ denote the spatial resolution of Φ . Given the L_2 -normalized global descriptors from the ground and aerial branches, the retrieval step is then performed to obtain C_k , a set of k aerial image candidates.

Localization Decoder. Given the detailed features of both the aerial candidate from C_k and I_g , the localization decoder predicts the possible location of I_g for metric localization by generating a dense probability distribution over the aerial candidate. To obtain a high-resolution localization distribution, we employ a hierarchical matching strategy inspired by [39]. This strategy involves iteratively refining the matching process between the ground descriptor and local regions in the aerial feature map, starting from a coarse resolution and

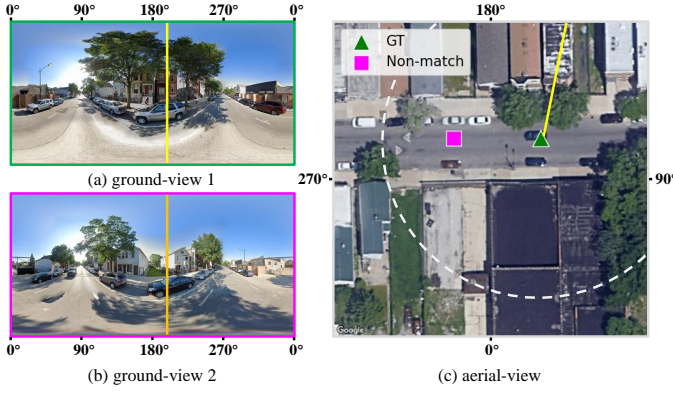


Fig. 3. Illustration of the geometric correspondence between aerial and ground views. The **green triangle** on the aerial image (c) corresponds to the ground-truth location of image (a), marked as GT, with a roughly matching field of view indicated by the white dashed line in (c). In contrast, the **magenta square** on (c) does not match (a), with its corresponding ground-view image shown in (b). Notably, the same azimuthal direction (yellow bar) in (a) and (c) displays the same scene, featuring trees and a red facade building. Conversely, the same azimuthal direction (orange bar) in (b) depicts a different scene, showing a white building.

progressively increasing the spatial detail. At each iteration, the matching score is used to inform the upsampling of the aerial features to a higher resolution.

Specifically, for the aerial branch, multi-scale features $\{F_a^i \mid i \in \{n, \dots, 0\}\}$ from the encoder and fine-grained extractor head are used for hierarchical matching. Corresponding detailed ground descriptors $\{f_g^i \mid i \in \{n, \dots, 0\}\}$ are generated through $n + 1$ projections of the ground detailed feature map $F_g^0 \in \mathbb{R}^{H' \times W' \times C}$. To enhance the generation of detailed ground descriptors, we follow [26], [39] to incorporate geometric constraints into the projector design, leveraging the fact [1] that pixels in the same azimuthal direction in aerial images typically correspond to vertical columns in ground-view images, as shown in the Fig. 3. By aggregating column-wise information from the ground feature maps, our projectors can capture scene details more effectively. Each projector comprises a 1×1 convolutional layer that reduces the feature channels, followed by a column-wise fully connected operation that summarizes the vertical information, thereby collapsing the column dimension from H' to 1. The resulting feature map is then reshaped into a compact 1D vector, yielding a detailed ground descriptor.

Next, hierarchical detailed feature matching starts from the lowest resolution at level 0 and moves toward level n . The initial score matrix \mathcal{M}^0 is computed by matching f_g^0 to F_a^0 , with LayerNorm and $L2$ -normalization being applied. Next, \mathcal{M}^0 is concatenated with the $L2$ -normalized F_a^0 and used to guide the upsampling of aerial features through deconvolution. Skip connections are added from previous aerial features for better scene layout information, followed by convolution to form the next-level matching feature maps. This process continues until level n is reached, generating matching scores $\{\mathcal{M}^i \mid i \in \{n, \dots, 0\}\}$. The highest-resolution score matrix with corresponding level- n feature maps are upsampled to the target resolution $L \times L \times 1$, and a softmax activation further converts it into a discrete distribution D . The Maximum A-

Posteriori (MAP) pixel location (\hat{x}, \hat{y}) in D yields the final location prediction.

D. Re-ranking Mechanism

In addition to retrieval and metric localization, we introduce a re-ranking mechanism that is essential to our hierarchical geo-localization pipeline. The purpose of re-ranking is to select the correct aerial image that covers the query location from the top- k retrieval candidates, thereby preventing erroneous location estimation from non-matching aerial images. Thanks to joint training with detailed features, UnifyGeo enables fine-grained comparisons between the query view and each retrieved aerial candidate for re-ranking.

Specifically, for each of the top- k aerial candidates $I_a^t \in \mathcal{C}_k$, we perform detailed feature matching with the query view to compute an initial score matrix \mathcal{M}_t^0 , using the same matching strategy as in the metric localization step². The re-ranking process is then formulated as:

$$I_a^* = \arg \max_{I_a^t \in \mathcal{C}_k} \left(s_t + \max_{(i,j)} \mathcal{M}_t^0(i,j) \right), \quad (4)$$

where s_t denotes the prior retrieval score of candidate I_a^t . Note that, each value in the score matrix \mathcal{M}_t^0 reflects the similarity between a specific region in the aerial image and the query ground-view, derived through detailed feature matching. For the aerial candidate that truly covers the query location, the highest-scoring position in its score matrix should correspond to the query location, as the detailed features here describe the same geographic area as the detailed query descriptor. We perform re-ranking by combining each candidate's maximum score from the initial score matrix with its retrieval score, thereby balancing overall layout and scene details. The aerial image with the highest combined score is selected as our re-ranking result.

E. Training Strategy for UnifyGeo

Our method aims to jointly retrieve the geographically matched aerial image for a given ground-level query image and accurately estimate the query location with the matched aerial as reference. To further improve retrieval performance, we incorporate a re-ranking process into the training pipeline. The multi-task loss function is defined as:

$$\mathcal{L} = \mathcal{L}_D + \alpha \mathcal{L}_G + \beta \mathcal{L}_M + \gamma \mathcal{L}_R, \quad (5)$$

where α , β and γ are hyperparameters during training. The individual components of the composite losses in Eq. 5 are detailed below.

Retrieval Loss. For image retrieval, we train the global descriptors extracted from both the aerial and ground branches using contrastive learning. To fully leverage the negative examples within the batch, we follow [18] to utilize the InfoNCE loss in a symmetric manner. This loss is designed to push the matched pairs closer in latent space and pull the

²In fact, we compute \mathcal{M}_t^0 only once for re-ranking and then reuse it in the localization decoder for metric localization.

unmatched pairs farther apart. The InfoNCE loss used for retrieval is formulated as:

$$\mathcal{L}_{\text{InfoNCE}} = -\log \frac{\exp(q \cdot r_+ / \tau)}{\sum_{i=1}^N \exp(q \cdot r_i / \tau)}, \quad (6)$$

where q represents the encoded query, r_+ and r_i denote the encoded positive reference images and negative samples, respectively, and τ is a learnable temperature parameter. For the symmetric InfoNCE loss, q can either be a ground image or an aerial image, depending on the direction of the information flow. Regardless of the direction, there is only one positive sample, r_+ , that corresponds to q . The loss \mathcal{L}_G is the average of the InfoNCE losses for both directions.

Localization Loss. For metric localization, we apply \mathcal{L}_D for location estimation, and \mathcal{L}_M for the detailed matching process. Specifically, we follow [39] to formulate the localization problem as a multi-class classification and apply a cross-entropy loss on the discrete probability distribution D . The ground truth location is represented by a discrete distribution D_{gt} with 2D Gaussian label smoothing of same size $L \times L$ with D . Then, \mathcal{L}_D is computed by:

$$\mathcal{L}_D = -\sum_{i=1}^L \sum_{j=1}^L D_{gt}^{i,j} \log D^{i,j}. \quad (7)$$

Since the localization probability distribution D is generated step by step by the matching score, we apply $\mathcal{L}_M = \sum_{l=0}^{l=n} \mathcal{L}_{M_l}$ on each matching score matrix of different levels. At level l , \mathcal{L}_{M_l} is used to encourage the aerial region descriptors $F_a^l(i, j)$ for locations close to the ground truth positions to match the detailed ground descriptor f_g^l . As for the ground truth of level l , we max-pool D_{gt} from $L \times L$ spatial dimensions to $L_l \times L_l$ resolution and renormalize it to generate weights $w_l^{i,j}$. The loss \mathcal{L}_{M_l} is finally defined as a weighted sum $\mathcal{L}_{M_l} = \sum_{i,j} w_l^{i,j} \mathcal{L}'_{M_l}(i, j)$ of InfoNCE loss based on cosine similarity,

$$\mathcal{L}'_{M_l}(i, j) = -\log \frac{\exp(\sin(f_g^l, F_a^l(i, j)) / \tau)}{\sum_{i', j'} \exp(\sin(f_g^l, F_a^l(i', j')) / \tau)}. \quad (8)$$

Re-ranking Loss. In our hierarchical geo-localization pipeline, the detailed feature matching matrix \mathcal{M}^0 plays a crucial role in the re-ranking process. During the metric localization phase, the loss \mathcal{L}_{M_0} is applied to \mathcal{M}^0 to ensure that this matrix effectively guides the generation of the discrete probability distribution. This loss encourages the highest matching score to correspond to the region in \mathcal{M}^0 that aligns with the ground camera's location. However, \mathcal{L}_{M_0} is constrained to a single aerial feature map with a resolution of $L' \times L'$, whereas the re-ranking process requires detailed matching score comparisons across multiple aerial images. To overcome this limitation, we introduce an additional supervision term \mathcal{L}_R on the matching matrix \mathcal{M}^0 . Specifically, during training, we extend the scope of comparison by matching each detailed ground descriptor f_g^0 against the feature maps F_a^0 of all aerial images within the mini-batch. This additional supervision encourages that the correct match location consistently achieve the highest matching score across all aerial detailed feature maps, thereby improving re-ranking effectiveness.

IV. EXPERIMENTS

In this section, we first introduce the three large-scale cross-view geo-localization datasets, evaluation metrics, and our implementation details. We then evaluate the localization accuracy of our UnifyGeo on the LF-CVGL task. Next, we compare the performance of UnifyGeo with state-of-the-art methods on the retrieval and metric localization tasks separately, demonstrating the effectiveness of our pipeline's components. Furthermore, we also provide qualitative results to show the differences between different methods. Finally, we conduct an extensive ablation study to validate our design choices and configurations.

A. Datasets

The VIGOR dataset [23] collects 90,618 aerial images covering 4 major cities in U.S.A, including New York City, San Francisco, Chicago, and Seattle. 105,214 street-view images with unique GPS locations are collected for query purposes. These data are balanced to ensure that each aerial image contains at most two positive street-view images. A positive pair means that the street-view image lies within the central quarter of the corresponding aerial image. To better simulate real-world conditions, for each positive pair, there are also three semi-positive aerial-view neighbors that cover regions of the street-view image, with the street-view image located around the periphery of these three aerial views. In addition to the ground truth of pairing relationships, the VIGOR dataset also provides the GPS coordinates of each query image and the offset relative to the center of the positive or semi-positive aerial image for meter-level localization evaluation. To better evaluate cross-view localization methods, the VIGOR dataset introduces two distinct evaluation protocols: same-area and cross-area splits. The same-area protocol assesses performance using images from all available cities, whereas the cross-area protocol evaluates generalization capabilities by training on images from New York and Seattle, and testing exclusively on data from San Francisco and Chicago. The resolution of aerial and street-view images in VIGOR is 640×640 and 1024×2048 , respectively. To ensure a fair comparison, we follow [18], [27] and use street-view images resized to 384×768 and aerial images resized to 384×384 as inputs for our method.

CVUSA and CVACT are two widely used datasets for evaluating the cross-view image retrieval task [29], [45]. Each dataset consists of 35,532 cross-view image pairs for training and 8,884 pairs for validation. Additionally, CVACT provides 92,802 test pairs with accurate geo-tags, referred to as CVACT_test, to assess the generalization ability of the evaluated model. Unlike VIGOR, these two datasets warp the panoramas to align with the center of the aerial images and adopt one-to-one retrieval for evaluation. During the experiments, we standardize the resolution of the cross-view images from both datasets to a consistent format, specifically 140×768 for the street-view images and 384×384 for the aerial-view images.

Notably, for the evaluation of LF-CVGL, we primarily use the VIGOR dataset, as it is, to our knowledge, the only

cross-view dataset capable of assessing model performance across large-scale scenes while also supporting fine-grained localization evaluation. In contrast, CVUSA and CVACT have coarse-grained paired labels, but their center-aligned cross-view image pairs enable precise geo-localization via successful top-1 retrieval. We therefore use these datasets as auxiliary evaluation benchmarks for LF-CVGL. Other metric localization datasets, such as KITTI [46] and Ford multi-AV [47], support fine-grained evaluation but are restricted to local localization and are not suitable for large-scale scenarios.

B. Evaluation Metrics

In our experiments, we evaluate three related tasks: LF-CVGL, image retrieval, and metric localization. For LF-CVGL, we adopt the evaluation metric from [23], which measures the percentage of query images localized within a certain distance (in meters) from the ground truth camera locations. On the VIGOR dataset, we consider two levels of localization accuracy: high-precision (1m), and coarse-precision (10m), denoted as “ $R@1m$ ” and “ $R@10m$ ” respectively. On the CVUSA and CVACT datasets, we report the LF-CVGL performance as the percentage of query images with the ground-truth aerial image ranked first in retrieval orders. For image retrieval, we use the top- k recall accuracy metric [1], [17], [18], denoted as “ $R@k$ ”. A retrieval is considered successful if the ground-truth aerial image is ranked within the top- k retrieved images for a given ground-level query image. On the VIGOR dataset, we also report the hit rate [23], which considers top-1 accuracy with both positive and semi-positive samples as correct results. For metric localization, we follow the evaluation protocol used in [23], [39] and report the mean and median errors (in meters) between predicted and ground-truth positions for all test image pairs.

C. Implementation Details

To balance encoding capability with parameter efficiency, the multi-granularity feature encoder in UnifyGeo is based on ConvNeXt-Tiny. We split ConvNeXt-Tiny (before the global average pooling layer) into two parts: the first three stages serve as the shared feature encoder, while Stage 4 is duplicated into two separate heads as the fine-grained feature extractor and the semantic feature extractor, without sharing parameters between these two extractors. Then, we retain only the first down-sampling layer and the ConvNeXt block in Stage 4 for constructing the extractor heads. In the feature aggregator, we halve the dimensions of \mathbf{Q} , \mathbf{K} , and \mathbf{V} , and then restore them before adding a residual connection to the input. This results in a global descriptor dimension of 768 after GeM pooling. For the localization decoder, hierarchical detailed feature matching is performed at 4 levels, with the lowest resolution of 12×12 at level 0. The number of feature channels and the dimensionality of the corresponding detailed ground descriptors are equal at each level, specifically 96, 192, 384, and 768.

For training, we follow [18] by applying a label smoothing of 0.1 in the retrieval InfoNCE loss. Consistent with [18] and [35], we also apply synchronized horizontal flipping and

TABLE I
COMPARISON OF METER-LEVEL LOCALIZATION ACCURACY WITH STATE-OF-THE-ART METHODS FOR LF-CVGL ON THE VIGOR DATASET.

Methods	Same-area		Cross-area	
	R@1m	R@10m	R@1m	R@10m
VIGOR [23]	0.55	25.50	0.06	6.20
PaSS-KD [27]	1.53	46.50	0.43	16.20
Sample4Geo [18]	0.24	20.84	0.23	17.81
Sample4Geo+CCVPE	29.90	73.10	18.61	56.71
Sample4Geo+HC-Net	35.92	74.91	19.28	59.23
UnifyGeo(ours)	39.64	81.37	25.58	66.24

rotation of cross-view image pairs, along with data augmentation techniques such as color jitter, grid dropout, and coarse dropout, to enhance model generalization. We set the hyperparameters α , β , and γ in the overall loss function to 100, 10, and 1, respectively. For efficient inference, the number of retrieved aerial image candidates, k , is empirically set to 5. All experiments are conducted with a batch size of 64 and trained for 40 epochs on each dataset. We use AdamW as the optimizer with a weight decay of 0.04 and an initial learning rate of $4.5e-4$, with a warm-up period of one epoch.

D. Comparison with State-of-the-art Methods

1) *LF-CVGL Experiments on VIGOR*: We conduct a comprehensive evaluation of our method on the LF-CVGL task using the VIGOR dataset, considering both same-area and cross-area settings, as presented in Table I. Our proposed UnifyGeo is compared against three state-of-the-art (SOTA) methods: VIGOR [23], PaSS-KD [27], and Sample4Geo [18]. Notably, the first two methods employ a retrieval-based approach followed by query location prediction, whereas Sample4Geo is a retrieval solution that achieves state-of-the-art retrieval performance. To ensure a more rigorous evaluation, we also introduce two stronger baselines that combine Sample4Geo with SOTA methods in metric localization, namely “Sample4Geo+CCVPE” and “Sample4Geo+HC-Net”. These combined baselines leverage Sample4Geo to retrieve the top-1 satellite image and then utilize CCVPE [39] or HC-Net [42] to predict the query location, forming a hierarchical geo-localization pipeline akin to our proposed method.

As shown in Table I, our method significantly outperforms all previous methods and combined baselines. Compared to the recent state-of-the-art LF-CVGL method PaSS-KD, UnifyGeo achieves 2 \times recall improvement at coarse precision (with a geo-location precision threshold of 10m) in the same-area setting, increasing to 4 \times recall gain for the cross-area setting. Furthermore, at a stringent geo-location precision threshold of 1m, our method demonstrates a localization recall rate exceeding 10-fold compared to PaSS-KD in both same-area and cross-area settings. These substantial improvements underscore the superiority of our proposed UnifyGeo. Furthermore, the results in Table I show that Sample4Geo presents a poor geo-localization performance across all metrics. However, when combined with metric localization approaches, the geo-localization performance can be improved by a large margin. This suggests that retrieval alone cannot perform accurate geo-

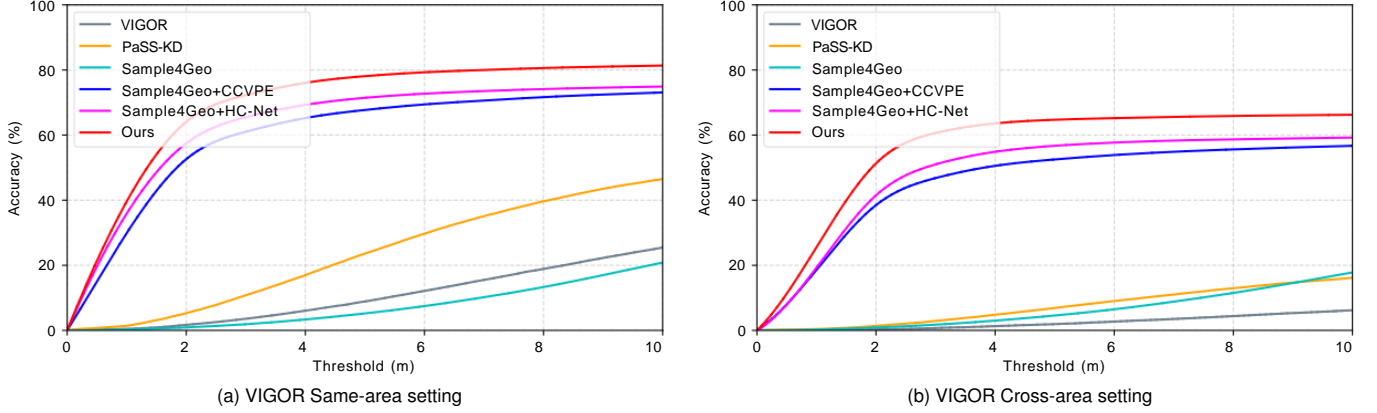


Fig. 4. Localization accuracy at various thresholds for the LF-CVGL task on the VIGOR dataset. Our method UnifyGeo is compared to the state-of-the-art methods and combined baselines on both the same-area (a) and cross-area (b) settings.

TABLE II

COMPARISON WITH STATE-OF-THE-ART METHODS FOR IMAGE RETRIEVAL ON THE VIGOR DATASET. THE BEST RESULTS ARE SHOWN IN **BOLDFACE** AND THE SECOND BEST RESULTS ARE UNDERLINED.

Methods	Same-area					Cross-area				
	R@1	R@5	R@10	R@1%	Hit Rate	R@1	R@5	R@10	R@1%	Hit Rate
SAFA [1]	33.93	58.42	68.12	98.24	36.87	8.20	19.59	26.36	77.61	8.85
VIGOR [17]	41.07	65.81	74.05	98.37	44.71	11.00	23.56	30.76	80.22	11.64
TransGeo [17]	61.48	87.54	91.88	<u>99.56</u>	73.09	18.99	38.24	46.91	88.94	21.21
PaSS-KD [27]	52.90	76.60	-	-	57.00	21.00	39.70	-	-	22.20
GeoDTR [35]	56.51	80.37	86.21	99.25	61.76	30.02	52.67	61.45	94.40	30.19
Sample4Geo [18]	<u>77.86</u>	95.66	97.21	99.61	89.82	<u>61.70</u>	83.50	88.00	98.17	69.87
UnifyGeo(ours)	82.80	<u>94.92</u>	<u>96.57</u>	99.47	88.72	67.58	<u>81.60</u>	<u>86.02</u>	<u>97.26</u>	68.24

TABLE III

COMPARISON WITH STATE-OF-THE-ART METHODS FOR METRIC LOCALIZATION ON THE VIGOR DATASET.

Methods	Same-area		Cross-area	
	Mean(m)	Median(m)	Mean(m)	Median(m)
CVR [23]	8.99	7.81	8.89	7.73
MCC [24]	6.94	3.64	9.05	5.14
SliceMatch [26]	5.18	2.58	5.53	2.55
GGCVT [48]	4.12	1.34	5.16	1.40
CCVPE [39]	3.60	1.36	4.97	1.68
HC-Net [42]	2.65	1.17	3.36	1.59
UnifyGeo(ours)	2.26	1.13	3.05	1.39

localization, while a hierarchical geo-localization pipeline can achieve more reasonable performance.

Notably, even with the improved performance achieved by the combined baselines, our method consistently yields superior results. Specifically, in terms of coarse precision, our method yields relative improvements of 8.6% (74.91% \rightarrow 81.37%) and 11.8% (59.23% \rightarrow 66.24%) over the best baseline, Sample4Geo+HC-Net, in the same-area and cross-area settings, respectively. For the cases with a high precision threshold, our method achieves relative improvements of 10.4% (35.92% \rightarrow 39.64%) in the same-area setting and 32.7% (19.28% \rightarrow 25.58%) in the cross-area setting, respectively. A comprehensive comparison of LF-CVGL performance is provided in Fig. 4. In addition to achieving superior performance, UnifyGeo also provides higher training efficiency and lower storage requirements compared to the

combined baseline. Notably, our model requires significantly fewer parameters (57.7M) compared to the second smallest model, Sample4geo+HC-Net (99.7M). This efficiency gain is attributed to our unified learning strategy, which enables shared feature computation and simultaneous multi-task training. These advantages make UnifyGeo more suitable for LF-CVGL in real-world scenarios, where efficient training and reduced storage requirements are crucial.

2) *Retrieval Experiments on VIGOR*: To quantitatively assess the retrieval performance of our geo-localization pipeline, we present a comparative analysis of our method against SOTA methods on the VIGOR dataset, as shown in Table II. Our method is competitive with Sample4Geo [18] and significantly outperforms other approaches. Notably, our UnifyGeo achieves substantial improvements over Sample4Geo at top-1 recall, with relative improvements of 6.3% (77.86% \rightarrow 82.80%) and 9.5% (61.70% \rightarrow 67.58%) in the same-area and cross-area settings, respectively. These improvements can be attributed to our effective re-ranking mechanisms. However, our method slightly underperforms Sample4Geo on other metrics, which may be due to our encoder design choices. Sample4Geo has shown that weight sharing between encoders yields better retrieval performance than using separate encoders for satellite and ground branches. In contrast, we employ distinct encoders for each branch to capture domain-specific features, which is beneficial to metric localization, a crucial component for LF-CVGL.

3) *Metric Localization Experiments on VIGOR*: To demon-

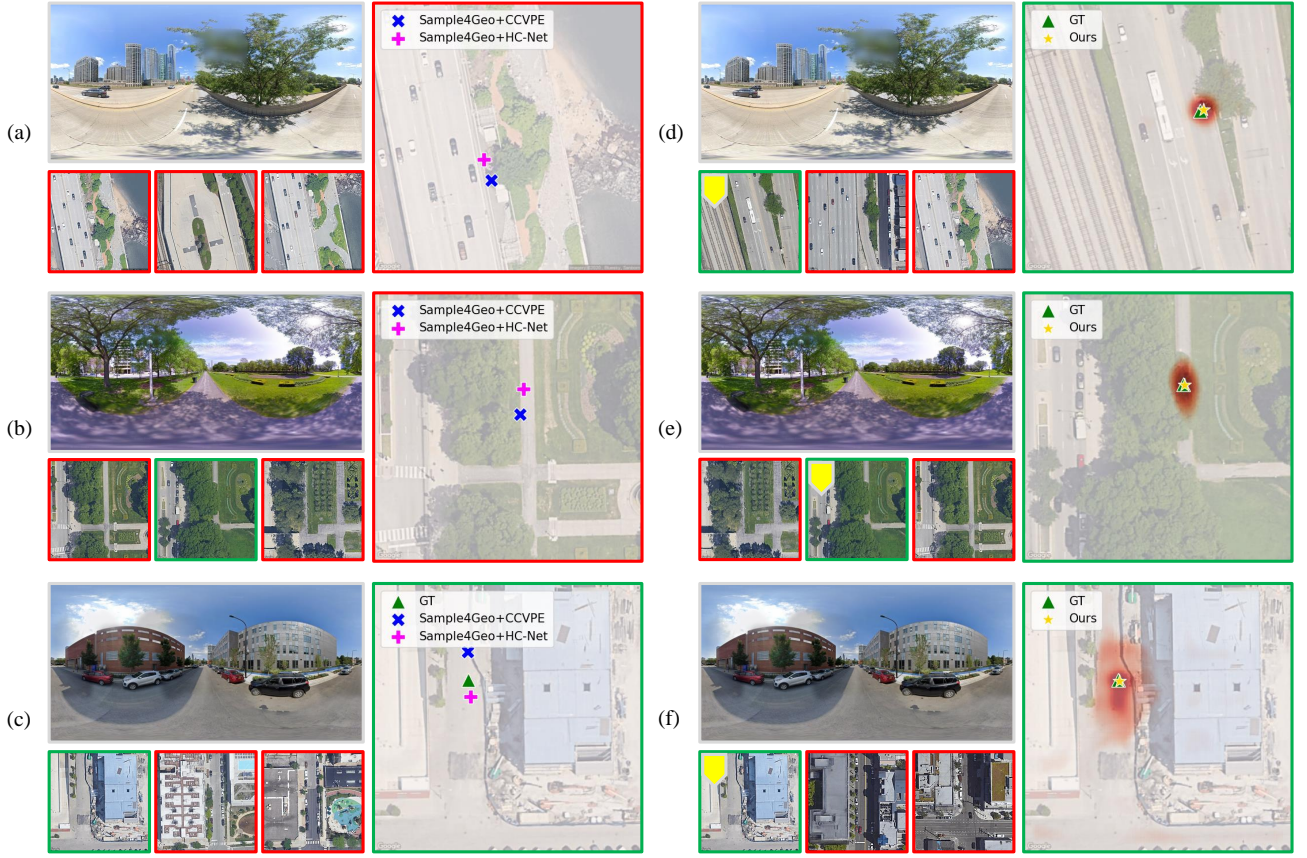


Fig. 5. Visualization of geo-localization methods on VIGOR. The left column (a-c) presents the results of two combined baselines, while the right column (d-f) shows the results of our method. Each row corresponds to the geo-localization results for the same query-view. Each panel of (a-f) comprises: a ground-view query image (top-left), the top-3 retrieved images (bottom-left, ordered from left to right), and a localization result based on the top-1 (or re-ranked) retrieved image (right, enlarged for clarity). Retrieved images are annotated with **light green** or **red** borders to indicate matches or non-matches with the query-view. In (d-f), a “**yellow pentagon**” on the top-left indicates the re-ranked candidate. Localization results are marked with distinct symbols: “**dark green triangle**” (ground-truth), “**blue cross**” (Sample4Geo+CCVPE), “**magenta plus**” (Sample4Geo+HC-Net), and “**golden star**” (our method).

TABLE IV

COMPARISON WITH STATE-OF-THE-ART METHODS FOR IMAGE RETRIEVAL ON THE CVUSA AND CVACT DATASETS. [†] REPRESENTS THAT POLAR TRANSFORMATION IS APPLIED TO AERIAL IMAGES. THE BEST RESULTS ARE SHOWN IN **BOLDFACE** AND THE SECOND BEST RESULTS ARE UNDERLINED.

Methods	CVUSA				CVACT-Val				CVACT-Test			
	R@1	R@5	R@10	R@1%	R@1	R@5	R@10	R@1%	R@1	R@5	R@10	R@1%
SAFA [†] [1]	89.84	96.93	98.14	99.64	81.03	92.80	94.84	98.17	55.50	79.94	85.08	94.49
SEH [†] [19]	95.11	98.45	99.00	99.78	84.75	93.97	95.46	98.11	-	-	-	-
TransGeo [17]	94.08	98.36	99.04	99.77	84.95	94.14	95.78	98.37	-	-	-	-
PaSS-KD [27]	94.09	98.42	99.13	99.77	87.20	94.30	95.67	97.85	66.81	88.03	90.87	98.02
GeoDTR [†] [35]	95.43	98.86	99.34	99.86	86.21	95.44	96.72	98.77	64.52	88.59	91.96	98.74
Sample4Geo [18]	98.68	99.68	99.78	99.87	<u>90.81</u>	96.74	97.48	98.77	<u>71.51</u>	<u>92.42</u>	94.45	<u>98.70</u>
UnifyGeo(ours)	98.91	<u>99.62</u>	99.72	99.84	91.38	<u>96.27</u>	<u>97.04</u>	98.45	73.42	92.46	<u>94.27</u>	98.43

strate the effectiveness of our metric localization, we compare the localization accuracy of our UnifyGeo with state-of-the-art methods in Table III. As shown, our method surpasses all these methods across all metrics, demonstrating exceptional performance in the metric localization task. Notably, compared to HC-Net [42], the second-best performer, our model achieves significant relative reductions of 37.2% and 16.8% in mean and median errors, respectively, in the same-area setting, and 38.6% and 17.3% in the cross-area setting. These substantial improvements highlight the benefits of our model design and unified learning strategy, which enable UnifyGeo to extract more informative latent patterns that facilitate accurate

localization. As a result, our superior location estimation performance leads to more accurate location predictions for successfully retrieved queries, ultimately enhancing the overall effectiveness of the LF-CVGL.

4) *LF-CVGL and Retrieval Experiments on CVUSA and CVACT*: To further evaluate our approach, we assess both the LF-CVGL and retrieval performance of our method on the CVUSA and CVACT datasets, and compare it with SOTA methods in Table IV. Given the center-aligned nature of the data, the top-1 recall rate serves as an effective metric for LF-CVGL. As shown in Table IV, our UnifyGeo achieves the best geo-localization performance. Notably, on the CVACT-

TABLE V
ABLATION STUDY FOR IMAGE RETRIEVAL ON THE VIGOR DATASET.

No.	Configurations				Same-area					Cross-area				
	UL	FA	Re-rank	\mathcal{L}_R	R@1	R@5	R@10	R@1%	Hit Rate	R@1	R@5	R@10	R@1%	Hit Rate
1.	-	-	-	-	74.12	93.44	95.62	99.48	85.43	51.73	74.63	80.74	96.80	58.10
2.	✓	-	-	-	75.54	94.08	96.15	99.51	86.53	53.99	76.31	82.26	96.98	60.57
3.	-	✓	-	-	77.19	94.31	96.20	99.45	87.68	58.83	80.10	85.01	97.28	65.90
4.	✓	✓	-	-	78.01	94.80	96.48	99.49	88.48	60.21	81.13	85.69	97.38	67.53
5.	✓	✓	-	✓	78.44	94.92	96.57	99.47	88.72	61.18	81.60	86.02	97.26	68.24
6.	✓	✓	✓	-	80.97	94.80	96.48	99.49	88.48	64.57	81.13	85.69	97.38	67.53
Ours	✓	✓	✓	✓	82.80	94.92	96.57	99.47	88.72	67.58	81.60	86.02	97.26	68.24

TABLE VI
ABLATION STUDY FOR METRIC LOCALIZATION ON THE VIGOR DATASET.

No.	Configurations			Same-area		Cross-area	
	UL	FA	\mathcal{L}_R	Mean(m)	Median(m)	Mean(m)	Median(m)
1.	-	-	-	2.59	1.00	4.30	1.50
2.	✓	-	-	2.63	1.18	4.22	1.43
3.	✓	✓	-	2.41	1.12	3.31	1.42
Ours	✓	✓	✓	2.26	1.13	3.05	1.39

test dataset, our method yields a relative improvement of 2.7% (71.51% \rightarrow 73.42%), demonstrating its superior generalization capabilities. In terms of retrieval performance, our method slightly underperforms on other metrics compared to Sample4Geo, consistent with the observations on the VIGOR dataset (Table II). We attribute this disparity to the same underlying factors. However, our method shows a significant advantage in $R@1$, which is crucial for applications like real-time geo-localization and navigation, where the accuracy of the top-ranked result is paramount.

E. Qualitative Analysis

To provide a more intuitive demonstration of our method’s effectiveness, we visualize the LF-CVGL results of our method and two combined baselines, “Sample4Geo+CCVPE” and “Sample4Geo+HC-Net”, on the VIGOR dataset in Fig. 5. The comparison highlights the superiority of our method in three distinct scenarios. Specifically, as shown in Fig. 5(a), our method successfully localizes the image, whereas the combined baselines fail to retrieve the correct reference. In Fig. 5(b), despite incorrect top-1 image initially retrieved by all methods, our method’s re-ranking mechanism enables correct selection of the satellite image and successful localization. Furthermore, in Fig. 5(c), even when all methods retrieve the correct image, our method outperforms the combined baselines in terms of localization accuracy, demonstrating its enhanced precision and reliability, and ultimately leading to more accurate geo-localization.

F. Ablation Studies

In this section, we demonstrate the effectiveness of our proposed components on VIGOR, including the Unified Learning Strategy (UL), Feature Aggregator (FA), Re-ranking process, and the re-ranking loss \mathcal{L}_R . To ensure a thorough analysis, we conduct ablation studies on all three tasks: image retrieval, metric localization, and LF-CVGL. The results of these evaluations are presented in Tables V, VI, and VII, respectively.

TABLE VII
ABLATION STUDY FOR LF-CVGL ON THE VIGOR DATASET.

No.	Configurations				Same-area		Cross-area	
	UL	FA	Re-rank	\mathcal{L}_R	R@1m	R@10m	R@1m	R@10m
1.	-	-	-	-	0.24	20.16	0.21	15.26
2.	-	✓	-	-	0.24	20.58	0.22	16.99
3.	✓	-	-	-	34.64	73.51	19.48	52.24
4.	✓	✓	-	-	36.63	76.07	21.88	58.46
5.	✓	✓	-	✓	37.37	76.74	22.81	59.63
6.	✓	✓	✓	-	38.48	79.47	23.98	63.17
Ours	✓	✓	✓	✓	39.64	81.37	25.58	66.24

For the metric localization baseline in Table VI, we train the detailed feature extraction pathway and the localization decoder. For baselines of the other two tasks, we train the global descriptor extraction pathway using average pooling for feature aggregation. The baseline results are provided in the first row of each table. Next, we examine the impact of each proposed component on both retrieval and metric localization tasks, followed by an analysis of its effects on the LF-CVGL task.

1) *Effects of UL*: As shown in Table V (rows No. 1 vs. 2), joint training with detailed features improves retrieval performance across all metrics compared to the baseline that only trains global descriptor extraction. A similar trend is also observed in Nos. 3 vs. 4. However, the metric localization task does not benefit from joint training of the two features, with only slight improvements in the cross-area settings but degradation in the same-area settings being observed, as shown in Table VI (Nos. 1 vs. 2). This issue is caused by training conflicts between different tasks in the shared encoder, as described in Section III, which will be analyzed when exploring the effect of FA. Notably, the detailed features extracted by UL can be leveraged as input to the localization decoder after the retrieval process, leading to a substantial improvement for LF-CVGL, as shown in Table VII (Nos. 1 vs. 3). Specifically, this step yields over 10-fold relative improvement in terms of $R@1m$ in the same-area setting and over 3-fold improvement in terms of $R@10m$ in the cross-area setting. These significant enhancements underscore that UL is the most significant factor in improving geo-localization performance compared to other proposed components.

2) *Effects of FA*: As shown in Table V, replacing average pooling with our proposed FA module consistently improves retrieval performance, regardless of whether UL is activated (Nos. 1 vs. 3 and Nos. 2 vs. 4). Furthermore, for the metric localization task in Table VI, applying FA significantly reduces localization error across all metrics, especially achieving a

21.6% relative reduction in mean error under the cross-area setting (Nos. 1-2 vs. 3). These results demonstrate the effectiveness of the FA module in mitigating training conflicts within the shared encoder, which is a key motivation for its proposal. By improving both retrieval and metric localization tasks, our FA module ultimately enhances the entire geo-localization performance, as shown in Table VII (No. 4), surpassing the configuration variants of Nos. 1-3. Notably, although FA improves retrieval performance (Nos. 1 vs. 3 in Table V), its effect on LF-CVGL is limited (Nos. 1 vs. 2 in Table VII). This suggests that enhancing retrieval alone is not sufficient to achieve highly accurate geo-localization results, highlighting the limitations of retrieval-based methods.

3) *Effects of Re-ranking*: In our LF-CVGL pipeline, re-ranking plays a crucial role in improving $R@1$ accuracy and informing metric localization. As shown in Table V (Nos. 4 vs. 6), re-ranking yields a relative improvement of 3.8% and 7.2% at $R@1$ metric in the same-area and cross-area settings, respectively. This enhancement contributes to the performance of LF-CVGL, yielding relative improvements of 5.1% and 9.6% in $R@1m$, as well as 4.5% and 8.1% in $R@10m$ metrics under the same-area and cross-area settings, respectively, as shown in Table VII (Nos. 4 vs. 6). These results highlight the effectiveness of re-ranking, which relies on detailed feature matching and further underscores the importance of our unified multi-granularity feature learning strategy.

4) *Effects of \mathcal{L}_R Loss*: The last two rows in Tables V and VI present the performance of our UnifyGeo framework before and after applying the \mathcal{L}_R loss. The results indicate that incorporating \mathcal{L}_R not only improves retrieval performance (with re-ranking) but also enhances metric localization accuracy. The improvement on the metric localization task can be attributed to the expansion of the comparison scope of detailed features from the image level to the mini-batch level. This expansion increases the number of negative samples in the InfoNCE loss calculation, thereby enhancing feature distinctiveness and enabling more accurate localization through improved initial matching scores. Furthermore, the use of \mathcal{L}_R also boots retrieval performance (without re-ranking), as seen in Table V (Nos. 4 vs. 5). This enhancement is due to the refinement of detailed features, which strengthens the shared encoder's ability to capture cross-view key patterns and improves the discriminative power of global descriptors. These mutually reinforcing improvements in retrieval and metric localization further highlight the effectiveness of our unified learning strategy. Ultimately, our method, which combines all proposed components, achieves the best LF-CVGL performance on both settings across all localization metrics, as shown in Table VII.

V. CONCLUSION

This paper proposes UnifyGeo, a unified hierarchical framework that integrates image retrieval and metric localization to achieve LF-CVGL in a coarse-to-fine manner. We improve the representations of both retrieval and metric localization tasks by employing a unified learning strategy, which establishes cross-task feature associations and complementary supervision within a shared encoder. In addition, we further enhance the

task coordination within UnifyGeo using a re-ranking mechanism, which provides better references for metric localization from retrieval candidates. Extensive experiments demonstrate the superiority of our proposed UnifyGeo framework on LF-CVGL, as well as its effectiveness on individual retrieval and metric localization tasks. As future works, we will investigate the potential benefits of integrating additional tasks, such as depth estimation and image synthesis, into our framework to further improve its geo-localization performance. We will also explore its adaptability to sequential ground images and optimize the framework for lightweight deployment, aiming to develop a universal geo-localization solution.

ACKNOWLEDGMENTS

This work was partially supported by the National Natural Science Foundation of China (No. 62372491), the Guangdong Basic and Applied Basic Research Foundation (2022B1515020103, 2023B1515120087), the Shenzhen Science and Technology Program (No. RCYX20200714114641140).

REFERENCES

- [1] Y. Shi, L. Liu, X. Yu, and H. Li, "Spatial-aware feature aggregation for image based cross-view geo-localization," in *Proceedings of Advances in Neural Information Processing Systems (NeurIPS)*, 2019, pp. 10 090–10 100.
- [2] Z. Song, X. Kang, X. Wei, S. Li, and H. Liu, "Unified and real-time image geo-localization via fine-grained overlap estimation," *IEEE Transactions on Image Processing (TIP)*, vol. 33, pp. 5060–5072, 2024.
- [3] J. Lin, Z. Luo, D. Lin, S. Li, and Z. Zhong, "A self-adaptive feature extraction method for aerial-view geo-localization," *IEEE Transactions on Image Processing (TIP)*, vol. 34, pp. 126–139, 2025.
- [4] M. Dai, E. Zheng, Z. Feng, L. Qi, J. Zhuang, and W. Yang, "Vision-based uav self-positioning in low-altitude urban environments," *IEEE Transactions on Image Processing (TIP)*, vol. 33, pp. 493–508, 2024.
- [5] A.-D. Doan, Y. Latif, T.-J. Chin, Y. Liu, T.-T. Do, and I. Reid, "Scalable place recognition under appearance change for autonomous driving," in *Proceedings of the IEEE/CVF International Conference on Computer Vision (ICCV)*, 2019, pp. 9318–9328.
- [6] D.-K. Kim and M. R. Walter, "Satellite image-based localization via learned embeddings," in *Proceedings of the International Conference on Robotics and Automation (ICRA)*, 2017, pp. 2073–2080.
- [7] P. Mirowski, M. Grimes, M. Malinowski, K. M. Hermann, K. Anderson, D. Teplyashin, K. Simonyan, K. Kavukcuoglu, A. Zisserman, and R. Hadsell, "Learning to navigate in cities without a map," in *Proceedings of Advances in Neural Information Processing Systems (NeurIPS)*, 2018.
- [8] A. Shetty and G. X. Gao, "Uav pose estimation using cross-view geo-localization with satellite imagery," in *Proceedings of the International Conference on Robotics and Automation (ICRA)*, 2019, pp. 1827–1833.
- [9] H.-P. Chiu, V. Murali, R. Villamil, G. D. Kessler, S. Samarasekera, and R. Kumar, "Augmented reality driving using semantic geo-registration," in *Proceedings of the IEEE Conference on Virtual Reality and 3D User Interfaces (VR)*, 2018, pp. 423–430.
- [10] X. Zou, Y. Yan, X. Hao, Y. Hu, H. Wen, E. Liu, J. Zhang, Y. Li, T. Li, Y. Zheng *et al.*, "Deep learning for cross-domain data fusion in urban computing: Taxonomy, advances, and outlook," *Information Fusion*, vol. 113, p. 102606, 2025.
- [11] W. Cheng, K. Chen, W. Lin, M. Goesele, X. Zhang, and Y. Zhang, "A two-stage outlier filtering framework for city-scale localization using 3d sfm point clouds," *IEEE Transactions on Image Processing (TIP)*, vol. 28, pp. 4857–4869, 2019.
- [12] L. Wang, S. Guo, W. Huang, Y. Xiong, and Y. Qiao, "Knowledge guided disambiguation for large-scale scene classification with multi-resolution cnns," *IEEE Transactions on Image Processing (TIP)*, vol. 26, pp. 2055–2068, 2017.
- [13] S. Cai, Y. Guo, S. Khan, J. Hu, and G. Wen, "Ground-to-aerial image geo-localization with a hard exemplar reweighting triplet loss," in *Proceedings of the IEEE/CVF International Conference on Computer Vision (ICCV)*, 2019, pp. 8391–8400.

- [14] Y. Shi, X. Yu, L. Liu, T. Zhang, and H. Li, "Optimal feature transport for cross-view image geo-localization," in *Proceedings of the AAAI Conference on Artificial Intelligence (AAAI)*, 2020, pp. 11 990–11 997.
- [15] J. Ye, Z. Lv, W. Li, J. Yu, H. Yang, H. Zhong, and C. He, "Cross-view image geo-localization with panorama-bev co-retrieval network," in *Proceedings of the European Conference on Computer Vision (ECCV)*, 2025, pp. 74–90.
- [16] S. Hu, M. Feng, R. M. Nguyen, and G. H. Lee, "Cvm-net: Cross-view matching network for image-based ground-to-aerial geo-localization," in *Proceedings of the IEEE/CVF Conference on Computer Vision and Pattern Recognition (CVPR)*, 2018, pp. 7258–7267.
- [17] S. Zhu, M. Shah, and C. Chen, "Transgeo: Transformer is all you need for cross-view image geo-localization," in *Proceedings of the IEEE/CVF Conference on Computer Vision and Pattern Recognition (CVPR)*, 2022, pp. 1162–1171.
- [18] F. Deuser, K. Habel, and N. Oswald, "Sample4geo: Hard negative sampling for cross-view geo-localisation," in *Proceedings of the IEEE/CVF International Conference on Computer Vision (ICCV)*, 2023, pp. 16 847–16 856.
- [19] Y. Guo, M. Choi, K. Li, F. Boussaid, and M. Bennamoun, "Soft exemplar highlighting for cross-view image-based geo-localization," *IEEE transactions on image processing (TIP)*, vol. 31, pp. 2094–2105, 2022.
- [20] Y. Xia, L. Zhang, Z. Liu, L. Nie, and X. Li, "Weakly supervised multimodal kernel for categorizing aerial photographs," *IEEE Transactions on Image Processing (TIP)*, vol. 26, no. 8, pp. 3748–3758, 2017.
- [21] J.-X. Cai, W. Feng, H.-X. Chen, and T.-J. Mu, "Sps: Accurate and real-time semantic positioning system based on low-cost dem maps," *IEEE Transactions on Image Processing (TIP)*, vol. 32, pp. 6401–6412, 2023.
- [22] S. Zhu, T. Yang, and C. Chen, "Visual explanation for deep metric learning," *IEEE Transactions on Image Processing (TIP)*, vol. 30, pp. 7593–7607, 2021.
- [23] Zhu, Sijie and Yang, Taojiannan and Chen, Chen, "Vigor: Cross-view image geo-localization beyond one-to-one retrieval," in *Proceedings of the IEEE/CVF Conference on Computer Vision and Pattern Recognition (CVPR)*, 2021, pp. 3640–3649.
- [24] Z. Xia, O. Booi, M. Manfredi, and J. F. Kooij, "Visual cross-view metric localization with dense uncertainty estimates," in *Proceedings of the European Conference on Computer Vision (ECCV)*, 2022, pp. 90–106.
- [25] Y. Shi and H. Li, "Beyond cross-view image retrieval: Highly accurate vehicle localization using satellite image," in *Proceedings of the IEEE/CVF Conference on Computer Vision and Pattern Recognition (CVPR)*, 2022, pp. 17 010–17 020.
- [26] T. Lentsch, Z. Xia, H. Caesar, and J. F. Kooij, "Slicematch: Geometry-guided aggregation for cross-view pose estimation," in *Proceedings of the IEEE/CVF Conference on Computer Vision and Pattern Recognition (CVPR)*, 2023, pp. 17 225–17 234.
- [27] S. Li, M. Hu, X. Xiao, and Z. Tu, "Patch similarity self-knowledge distillation for cross-view geo-localization," *IEEE Transactions on Circuits and Systems for Video Technology (TCSVT)*, vol. 34, pp. 5091–5103, 2023.
- [28] T.-Y. Lin, Y. Cui, S. Belongie, and J. Hays, "Learning deep representations for ground-to-aerial geolocalization," in *Proceedings of the IEEE/CVF Conference on Computer Vision and Pattern Recognition (CVPR)*, 2015, pp. 5007–5015.
- [29] S. Workman, R. Souvenir, and N. Jacobs, "Wide-area image geolocalization with aerial reference imagery," in *Proceedings of the IEEE/CVF International Conference on Computer Vision (ICCV)*, 2015, pp. 3961–3969.
- [30] M. Bansal, H. S. Sawhney, H. Cheng, and K. Daniilidis, "Geo-localization of street views with aerial image databases," in *Proceedings of the 19th ACM international conference on Multimedia (ACM MM)*, 2011, pp. 1125–1128.
- [31] A. Viswanathan, B. R. Pires, and D. Huber, "Vision based robot localization by ground to satellite matching in gps-denied situations," in *Proceedings of the IEEE/RSJ International Conference on Intelligent Robots and Systems (IROS)*, 2014, pp. 192–198.
- [32] R. Arandjelovic, P. Gronat, A. Torii, T. Pajdla, and J. Sivic, "Netvlad: Cnn architecture for weakly supervised place recognition," in *Proceedings of the IEEE/CVF Conference on Computer Vision and Pattern Recognition (CVPR)*, 2016, pp. 5297–5307.
- [33] J. Lin, Z. Zheng, Z. Zhong, Z. Luo, S. Li, Y. Yang, and N. Sebe, "Joint representation learning and keypoint detection for cross-view geo-localization," *IEEE Transactions on Image Processing (TIP)*, vol. 31, pp. 3780–3792, 2022.
- [34] H. Yang, X. Lu, and Y. Zhu, "Cross-view geo-localization with layer-to-layer transformer," in *Proceedings of Advances in Neural Information Processing Systems (NeurIPS)*, 2021, pp. 29 009–29 020.
- [35] X. Zhang, X. Li, W. Sultani, Y. Zhou, and S. Wshah, "Cross-view geo-localization via learning disentangled geometric layout correspondence," in *Proceedings of the AAAI Conference on Artificial Intelligence (AAAI)*, 2023, pp. 3480–3488.
- [36] Y. Zhu, H. Yang, Y. Lu, and Q. Huang, "Simple, effective and general: A new backbone for cross-view image geo-localization," *arXiv preprint arXiv:2302.01572*, 2023.
- [37] M. Shugaev, I. Semenov, K. Ashley, M. Klaczynski, N. Cuntoor, M. W. Lee, and N. Jacobs, "Arcgeo: Localizing limited field-of-view images using cross-view matching," in *Proceedings of the IEEE/CVF Winter Conference on Applications of Computer Vision (WACV)*, 2024, pp. 209–218.
- [38] G. Li, M. Qian, and G.-S. Xia, "Unleashing unlabeled data: A paradigm for cross-view geo-localization," in *Proceedings of the IEEE/CVF Conference on Computer Vision and Pattern Recognition (CVPR)*, 2024, pp. 16 719–16 729.
- [39] Z. Xia, O. Booi, and J. F. Kooij, "Convolutional cross-view pose estimation," *IEEE Transactions on Pattern Analysis and Machine Intelligence (TPAMI)*, vol. 46, pp. 3813–3831, 2023.
- [40] Z. Chen, K. Li, H. Li, Z. Fu, H. Zhang, and Y. Guo, "Metric localization for lunar rovers via cross-view image matching," *Visual Intelligence (VI)*, vol. 2, p. 12, 2024.
- [41] F. Fervers, S. Bullinger, C. Bodensteiner, M. Arens, and R. Stiefelhagen, "Uncertainty-aware vision-based metric cross-view geolocalization," in *Proceedings of the IEEE/CVF Conference on Computer Vision and Pattern Recognition (CVPR)*, 2023, pp. 21 621–21 631.
- [42] X. Wang, R. Xu, Z. Cui, Z. Wan, and Y. Zhang, "Fine-grained cross-view geo-localization using a correlation-aware homography estimator," in *Proceedings of Advances in Neural Information Processing Systems (NeurIPS)*, 2024, pp. 5301–5319.
- [43] F. Radenović, G. Tolias, and O. Chum, "Fine-tuning cnn image retrieval with no human annotation," *IEEE transactions on pattern analysis and machine intelligence (TPAMI)*, vol. 41, pp. 1655–1668, 2018.
- [44] T. Ng, V. Balntas, Y. Tian, and K. Mikołajczyk, "Solar: second-order loss and attention for image retrieval," in *Proceedings of the European Conference on Computer Vision (ECCV)*, 2020, pp. 253–270.
- [45] L. Liu and H. Li, "Lending orientation to neural networks for cross-view geo-localization," in *Proceedings of the IEEE/CVF Conference on Computer Vision and Pattern Recognition (CVPR)*, 2019, pp. 5624–5633.
- [46] A. Geiger, P. Lenz, C. Stiller, and R. Urtasun, "Vision meets robotics: The kitti dataset," *The international journal of robotics research (IJRR)*, vol. 32, pp. 1231–1237, 2013.
- [47] S. Agarwal, A. Vora, G. Pandey, W. Williams, H. Kourous, and J. McBride, "Ford multi-av seasonal dataset," *The International Journal of Robotics Research (IJRR)*, vol. 39, pp. 1367–1376, 2020.
- [48] Y. Shi, F. Wu, A. Perincherry, A. Vora, and H. Li, "Boosting 3-dof ground-to-satellite camera localization accuracy via geometry-guided cross-view transformer," in *Proceedings of the IEEE/CVF International Conference on Computer Vision (ICCV)*, 2023, pp. 21 516–21 526.